

Modelling and Analysis of UV Laser Micromachining of Copper

W. Zhang, Y. L. Yao and K. Chen

Department of Mechanical Engineering, Columbia University, New York, USA

UV laser micromachining of metallic materials has been used in microelectronic and other industries. Knowledge and data about the process vary with feature size, material, laser wavelength and pulse duration. This paper reports on experimental and numerical investigation of micromachining of copper using a frequency tripled Nd:YAG laser with 50 ns pulse duration. An axisymmetric model is developed which allows consideration of laser beam distribution and its coupling with the target material. This is important for the process where the removal extent is in the same order of the removal depth. The model uses an enthalpy method to track the solid/liquid interface. Stefan and kinetic boundary conditions are applied at the liquid–vapour interface, and property discontinuity across the Knudsen layer is considered. Relevant experimental results are also presented and compared with the model predicted results. The range of thermal vaporisation dominated machining of copper using nanosecond time scale lasers was studied, and optimum laser intensity for micromachining of copper was suggested.

Keywords: Ablation; UV laser micromachining

1. Introduction

Laser micromachining is an established method for production of high-precision features such as via formation, especially in the microelectronic industry. The quality and profile of drilled holes have drawn increasing attention because of the decreasing size and higher level of integration. UV lasers have been widely used for this purpose owing to their better absorption. Using Q-Switch techniques, they offer short pulse duration and high peak power, which limits the heat affected zone and makes the material removal process be dominated by ablation. Excimer lasers and frequency-tripled Nd:YAG lasers are among the most popular. Although copper is an important material in

many applications, detailed study on laser machining of copper at micron level is not readily available.

Experimental work was carried out to investigate the laser ablation processes in order to understand the physics of laser material interactions. The process of thin Cu film removal at a wavelength of 532 nm was studied [1] and the effects of laser intensity on ablation mechanism were revealed. The thin film selective multishot ablation at 248 nm was also investigated [2]. A systematic review of experimental results involving UV lasers can be found in [3]. Many models of laser drilling have also been developed. Paek developed a theoretical model to predict the temperature profile assuming a laser beam of circular cross-section and uniform intensity [4]. Dabby calculated the transient temperature and penetrating velocity during the vaporisation process [5]. The models more recently developed [6,7] considered the effects of gas dynamics and Knudsen layer discontinuity during the ablation process. These models assume 1D heat transfer in target material, recognising that the machining depth is much smaller than the diameter of the hole, which is reasonable for relatively large holes (a few hundred μm). As a result, however, the effects of beam profiles and cavity profiles are not considered. These factors are important when the size of the hole is comparable to the drilling depth. Modest developed a transient 3D heat conduction model for material volume being machined [8]. However, the model assumes that vaporisation occurs in a single step without melting. Gas dynamics and the discontinuity layer were not taken into account. This is not suitable for laser machining of metals on a nanosecond time scale. Other models have been developed to study the phenomena of vapour plume and plasma during laser–plasma–solid interactions [9,10], some of which were developed for the application of thin-film deposition via laser ablation.

The model in this paper concentrates on the heat transfer and associated phase changes inside the target material, which is of major concern in machining applications. Stefan and kinetic boundary conditions are applied at the liquid–vapour interface, and property discontinuity across the Knudsen layer is considered. Heat conduction is calculated using an enthalpy method. Most importantly, the axisymmetric model allows consideration of laser beam distribution and its coupling with the target material, which is important when the ablation extent is in the same order as the ablation depth. The model is

Correspondence and offprint requests to: Dr L. Yao, Department of Mechanical Engineering, Columbia University, 220 S. W. Mudd, Mail Code 4703, 500 West 120th Street, New York, NY 10027, USA. E-mail: ylyl@columbia.edu

capable of simulating the formation of a cavity under the irradiation of pulsed UV laser beams with laser intensities of less than $5 \times 10^9 \text{ W cm}^{-2}$. Relevant experiments were also carried out.

2. Physical Considerations in UV Laser Micromachining

The characteristic penetration depth of copper is 14.6 nm for the 355 nm wavelength (see Appendix, point 1). This indicates that copper and UV laser interaction is a surface phenomenon. For the concept of temperature to be valid, the acting volume should be in thermodynamic equilibrium and be of macroscopic size, thus the internal energy fluctuation should be small. The internal energy fluctuation for copper–laser interaction with a beam size of $4.5 \mu\text{m}$ can be computed to be around 2.44×10^{-9} (Appendix point 2), so the system can be considered macroscopic. The electron relaxation time τ_e for copper is 7×10^{-17} s. The time for energy transfer from electron to lattice $\tau_{lattice}$ is of the order of 10^{-12} s. So, for the 50 ns pulse duration time, which is about 50 000 times the $\tau_{lattice}$, the electron-gas temperature and the lattice temperature in the target material are about the same, and thermal equilibrium can be assumed. In conclusion, traditional heat transfer concepts can be safely applied for UV laser machining using pulses in the nanosecond time scale.

The mechanism of laser ablation of materials is dependent on laser intensity. Assuming equilibrium vaporisation conditions with vapour pressure at 1 atm., it was found that copper has a linear evaporation rate of $7.3 \times 10^{-3} \text{ m s}^{-1}$ [11]. For a 50 ns laser pulse, the depth of ablation per pulse is 3.65×10^{-10} m. This gives the upper limit of ablation depth through pure evaporation. If the experimental ablation depth is close to this limit, the ablation is thermal equilibrium evaporation dominated and the fluid motion effect is weak. If the experimental ablation depth is far beyond this limit, hydrodynamic ablation dominates. Relevant information about copper–laser interaction is listed in the Appendix point 3.

3. Modelling Background

Under the irradiation of a laser beam, the target material is first heated from room temperature to melting temperature. Depending on laser intensity and material properties, the molten part of material will be evaporated by additional heating when it reaches the vaporisation point and a vapour-filled cavity is formed (Fig. 1). A thin, so-called Knudsen layer exists at the melt–vapour interface, where the state variables undergo discontinuous changes across the layer [12]. When the incident laser intensity exceeds a certain threshold, vaporisation leads to plasma formation, which will absorb a certain percentage of laser energy. The more the intensity exceeds the threshold, the denser the plasma, and the greater the percentage of absorption. In practice, an assisting gas jet could disperse the plasma plume sideward and lower the plasma density. However, the plasma effects still exist. By introducing a correction

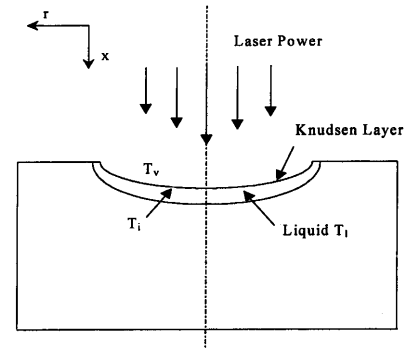


Fig. 1. Calculation domain.

coefficient in the modelling of laser intensity, the plasma effects are corrected. The motion of molten material caused by the Marangoni effect [13] is neglected.

The governing equation for energy balance can be written as

$$\frac{\partial h}{\partial t} + \frac{\partial \Delta H}{\partial t} = \frac{\partial}{\partial x} \left(\alpha \frac{\partial h}{\partial x} \right) + \frac{1}{r} \frac{\partial}{\partial r} \left(r \alpha \frac{\partial h}{\partial r} \right) \quad (1)$$

where α is heat diffusivity and ρ is density, x and r are distances along axial and radial directions, as shown in Fig. 1. The enthalpy of the material (the total heat content) can be expressed as $H = h + \Delta H$, i.e. the sum of sensible heat, $h = c_p T$ (c_p is the heat capacity, and T is the temperature), and latent heat ΔH . It either varies with L_m , the latent heat for melting, or is zero. The enthalpy formulation allows the melting boundary to be traced as a function of time without regeneration of the calculation grids [14].

At the melt–vapour front, the Stefan boundary condition is applied,

$$Q + k \left(\frac{\partial T}{\partial x} + r \frac{\partial T}{\partial r} \right) + \rho_l v_l L_v - \rho_v v_v (c_p T_i + E_v) = 0$$

$$E_v = \frac{RT_v}{(\gamma - 1)M_v} + \frac{1}{2}v_v^2,$$

$$Q = C(1 - Rl)I(t) \exp(-\gamma^2/b^2) \exp(-\beta x) \quad (2)$$

where Q is the laser heat flux which depends on the reflectivity Rl , absorptivity β and the plasma correction coefficient C . I is the laser intensity which is a function of time, and b is the laser beam radius. The subscripts l , v , and i denote liquid phase, vapour phase, and vapour–liquid interface, respectively. The gas energy E_v includes the internal energy and the kinetic energy. k is the heat conductivity, v the velocity, R the universal gas constant, γ the specific heat ratio, L_v the latent heat of vaporisation, and M_v the molecular mass. The velocity, the laser energy flux and the heat conduction flux are given along the normal direction of the cavity profile. The vapour–liquid front is determined by tracing the temperature. As long as the temperatures at certain grid points reach vaporisation temperature, the grids which have temperatures larger than vaporisation temperature are taken as the gas phase, and the calculation starts from the newly determined vapour–liquid front.

A photodiode sensor is used to record the actual temporal distribution of the laser intensity. In simulation, $I(t)$ takes the

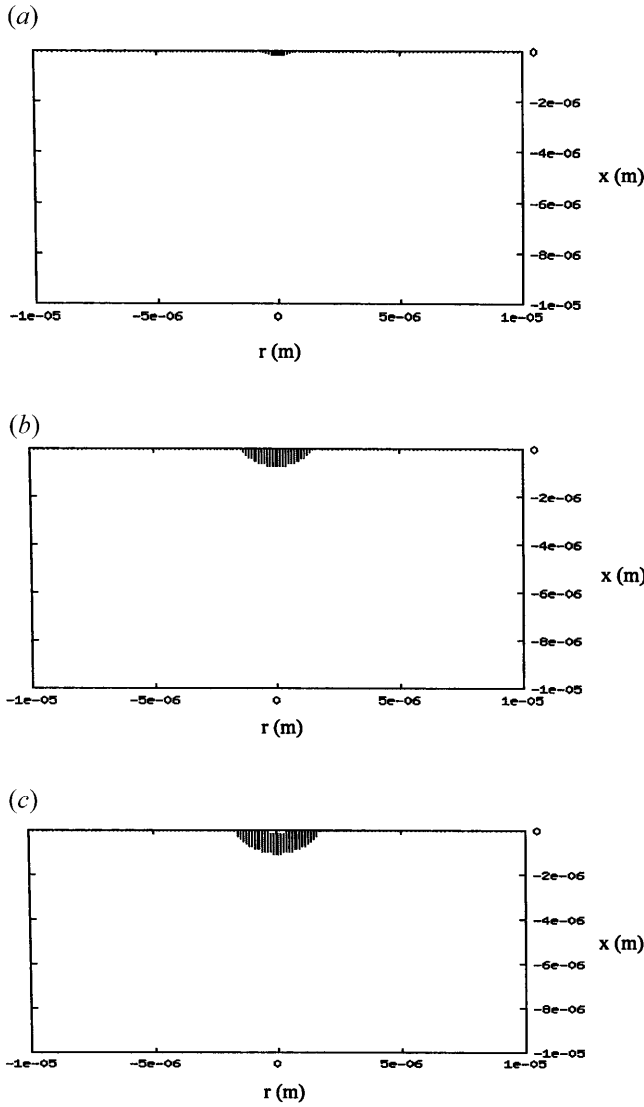


Fig. 2. Cavity profiles at the end of a 50 ns laser pulse. (a) $I = 4 \times 10^7 \text{ W cm}^{-2}$; (b) $I = 8 \times 10^7 \text{ W cm}^{-2}$; (c) $I = 1.15 \times 10^8 \text{ W cm}^{-2}$. Wavelength $\lambda = 355 \text{ nm}$, Gaussian beam, beam radius $b = 2.25 \mu\text{m}$, Cu. Vertical lines denote molten layer.

interpolated values at the current time. The plasma correction coefficient C is decided as follows.

$$C = 1 \quad \text{if } I(t) < I_c$$

$$C = 0.62927 - 0.5 \tanh \frac{I - 2.4(I_{strong} - I_c)}{2.4(I_{strong} - I_c)} \quad \text{if } I_c \leq I(t) < 1.8 \times I_{strong}$$

$$C = 0.7118 \quad \text{if } I(t) \geq 1.8 \times I_{strong} \quad (3)$$

where I_c is the critical plasma generation value and I_{strong} is the strong plasma generation value. For copper at 355 nm, $I_c = 5 \times 10^8 \text{ W cm}^{-2}$, $I_{strong} = 5 \times 10^9 \text{ W cm}^{-2}$, then $C = 0.87$ at $I = I_{strong}$.

The reflectivity for UV wavelengths is

$$Rl = \frac{(n-1)^2 + k^2}{(n+1)^2 + k^2} \quad (4)$$

where n and k are indices of refraction and extinction coef-

ficients. For pure copper at a wavelength $\lambda = 0.355 \mu\text{m}$, $n = 1.34$, and $k = 1.93$, the absorption coefficient is given by

$$\beta = \frac{4\pi k}{\lambda} \quad (5)$$

The following analytic relationships [12] are applied to account for the discontinuity of the Knudsen layer.

$$\frac{T_{vi}}{T_{li}} = \left[\sqrt{1 + \pi \left(\frac{m \gamma - 1}{2 \gamma + 1} \right)^2} - \sqrt{\pi} \frac{m \gamma - 1}{2 \gamma + 1} \right]^2$$

$$\frac{\rho_{vi}}{\rho_{li}} = \sqrt{\left(\frac{T_{li}}{T_{vi}} \right)} \left[(m^2 + \frac{1}{2}) \exp(m^2) \operatorname{erfc}(m) - \frac{m}{\sqrt{\pi}} \right]$$

$$+ \frac{1}{2} \frac{T_{li}}{T_{vi}} [1 - \sqrt{\pi} m \exp(m^2) \operatorname{erfc}(m)]$$

$$\exp(m^2) \operatorname{erfc}(m) \approx 0.34802a - 0.09588a^2 + 0.74786a^3$$

$$a = 1/(1 + 0.47047m), \quad m = \frac{v_{vi}}{\sqrt{(2RT_{vi}/Ma_v)}} \quad (6)$$

where subscript vi denotes the values of the vapour adjacent to the Knudsen layer and li the values of liquid adjacent to the Knudsen layer. Ma_v is the vapour Mach number, and $\operatorname{erfc}(m)$ the complementary error function.

The gas velocity is obtained from mass conservation:

$$\rho_i v_i = \rho_v (v_i + v_v) \quad (7)$$

where v_i is the velocity of the melt–vapour interface and v_v is the vapour velocity.

The boundary conditions given by Eq. (2) depend on the vapour temperature, which is back-related to the vapour–liquid interface temperature through Eq. (6). Some thermal properties of copper are treated as temperature sensitive. The calculation process is thus iterative between the gas, liquid, and solid phase until proper convergence is achieved. The properties used in simulation are listed in the Appendix point 4.

A control-volume-based computation scheme was developed to solve the coupled governing equations. The 2D discrete equations are written in the fully implicit form. The coefficients of variables are linearised between each time step to facilitate the convergence. The computational domain is taken large enough (5 times the beam radius in both the x and r directions) so that the temperatures at the external boundaries can be considered to be at room temperature. The convective and radiative heat transfer on the top surface is negligible compared with conduction heat loss and thus is not considered.

4. Experimental Set-up and Beam Property Analysis

A Q-switched Nd:YAG laser with its fundamental frequency tripled ($\lambda = 355 \text{ nm}$) and 50 ns pulse duration was used as the UV energy source for the experiments. The laser micromachining system includes the UV laser source, polariser, beam collimator, optical focus systems, CCD camera, TV monitor, micrometer table, and control software. A polariser is used to adjust the laser intensity without affecting the stable operation

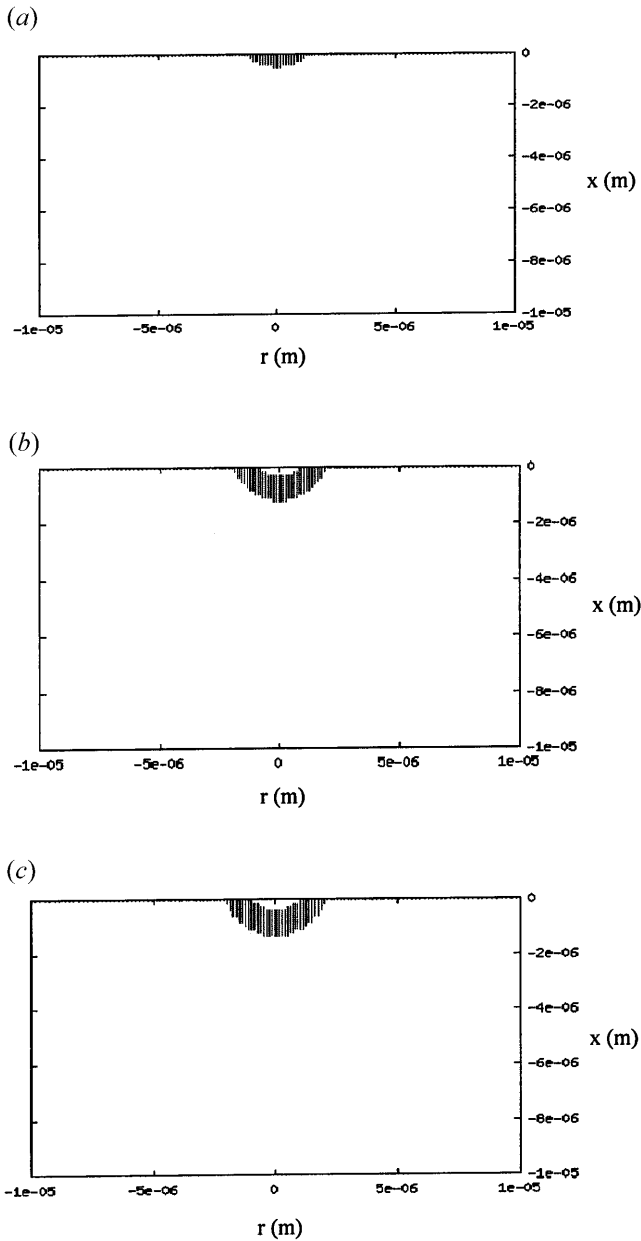


Fig. 3. Time history of cavity profiles at $I = 1.7 \times 10^8 \text{ W cm}^{-2}$. (a) $t = 10 \text{ ns}$; (b) $t = 30 \text{ ns}$; (c) $t = 50 \text{ ns}$. Wavelength $\lambda = 355 \text{ nm}$, Gaussian beam, beam radius $b = 2.25 \text{ }\mu\text{m}$, Cu. Vertical lines denote molten layer.

of the laser source and a beam collimator is used to collimate and expand the beam for minimum focused spot size. A photon diode sensor is used to monitor the output laser pulses in real time. Copper foils of 99.9% purity and 0.3 mm thickness were polished before laser machining.

The focused laser beam size is required for laser intensity computation, but it is usually difficult to measure the focused beam directly, especially for cases when the focused spot size is below $10 \text{ }\mu\text{m}$. Experimental measurements were combined with optical calculations to overcome this difficulty. The spot size out of the collimator, which is several millimetres, was

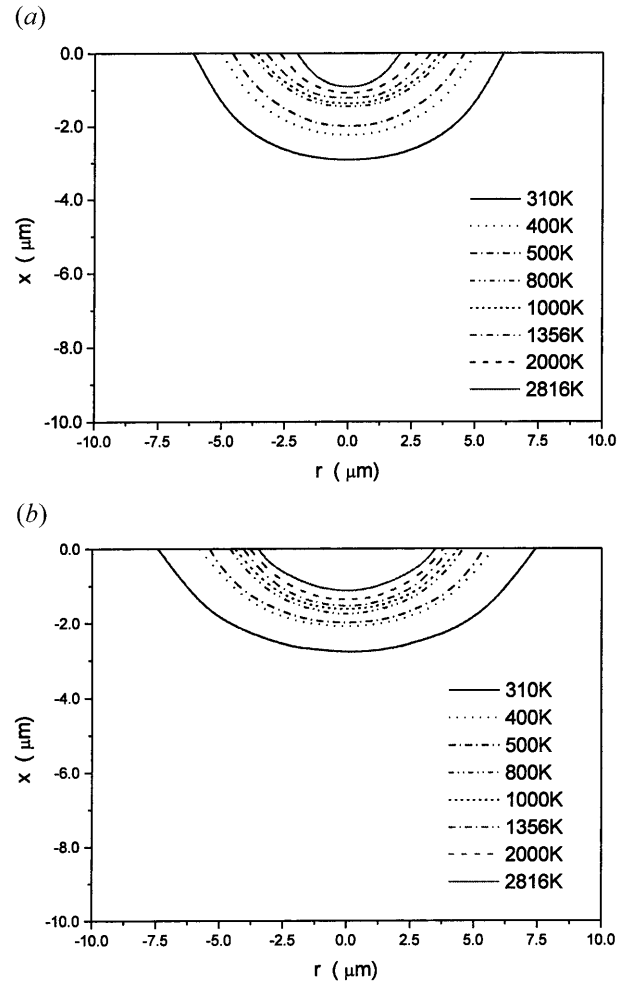


Fig. 4. Temperature contours at the end of a 50 ns laser pulse. (a) $I = 6 \times 10^8 \text{ W cm}^{-2}$; (b) $I = 1.5 \times 10^9 \text{ W cm}^{-2}$. Wavelength $\lambda = 355 \text{ nm}$, Gaussian beam, beam radius $b = 2.25 \text{ }\mu\text{m}$, Cu.

measured. For such a dimension and intensity, the knife-edge method was readily applied. Three measurements at different distances from the collimator were taken to obtain (Z_n, D_n) , $n = 1, 2, 3$, where D_n is the beam size at location Z_n . The laser beams satisfy the following equation [15,16]:

$$D_n^2 = D_0^2 + \left(\frac{4M^2\lambda}{\pi} \right)^2 \frac{(Z_n - Z_0)^2}{D_0^2} \quad (n = 1, 2, 3) \quad (8)$$

where D_0 is the beam waist, Z_0 is the beam waist location, and M^2 is the beam quality parameter to be determined. When M^2 is known, the beam divergence, focused spot size, and depth of focus (DOF) can be calculated quickly. For the laser used, it was found that $M^2 = 1.497$, minimum beam size $D_{min} = 4.558 \text{ }\mu\text{m}$, divergence at large distance $\theta_{infinity} = 44.96 \text{ }\mu\text{rad}$, and $DOF = \pm 9.822 \text{ }\mu\text{m}$.

5. Results and Discussions

The computation domain of simulation is five times the beam radius in both the x -direction and r -direction. Uneven grids

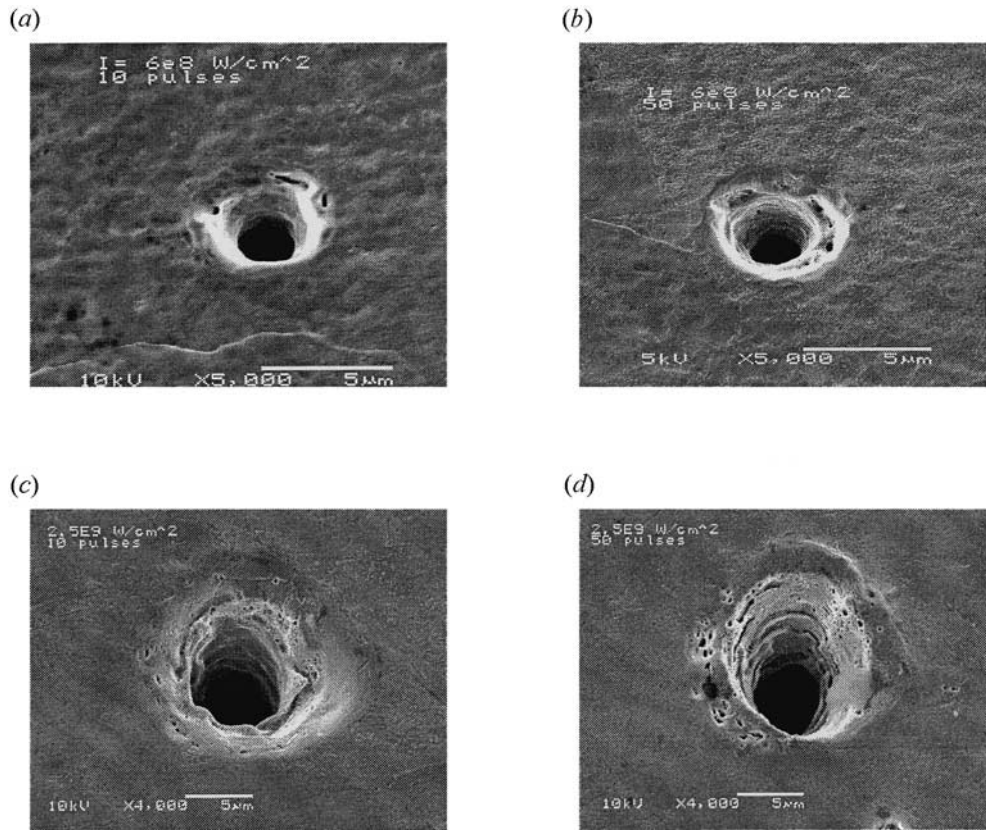


Fig. 5. SEM micrographs of laser drilled holes. (a) $I = 6 \times 10^8 \text{ W cm}^{-2}$, 10 pulses; (b) $I = 6 \times 10^8 \text{ W cm}^{-2}$, 50 pulses; (c) $I = 2.5 \times 10^9 \text{ W cm}^{-2}$, 10 pulses; (d) $I = 2.5 \times 10^9 \text{ W cm}^{-2}$, 50 pulses. Wavelength $\lambda = 355 \text{ nm}$, Gaussian beam, beam radius $b = 2.25 \text{ }\mu\text{m}$, pulse duration 50 ns, repetition rate 2 kHz, Cu.

are used with denser grids near the centre and the top, and the number of grids is 120×120 . The laser beam intensity has a Gaussian distribution with a $1/e^2$ beam radius $b = 2.25 \text{ }\mu\text{m}$. The time step is 10 ns and the temperature field is considered to be converged when the relative error is less than 10^{-5} . From the simulation, cavity geometry, temperature distribution and melting surface recessing speed are predicted.

Figure 2 shows the simulation results of the cavity profile at the end of a 50 ns pulse at different levels of beam intensities. The material starts melting at $4 \times 10^7 \text{ W cm}^{-2}$ (Fig. 2(a)). The material starts vaporising at $9.8 \times 10^7 \text{ W cm}^{-2}$ and at $1.15 \times 10^8 \text{ W cm}^{-2}$ a cavity on top is visible (Fig. 2(c)). Between these conditions, pure melting evolves (Fig. 2(b)). The vertical lines denote the molten layer. Figure 3 shows the time history of the cavity profile with $I = 1.7 \times 10^8 \text{ W cm}^{-2}$. It can be seen that at 10 ns, melting has appeared but there is no vaporisation. At 30 ns, part of the material is vaporised and a visible cavity is formed with more molten copper beneath it. At 50 ns, the cavity further widens and deepens.

Figure 4 shows the temperature contours in the material after 50 ns for the intensity of $6 \times 10^8 \text{ W cm}^{-2}$ and $1.5 \times 10^9 \text{ W cm}^{-2}$. It can be seen that the temperature drops quickly to room temperature at a distance of about three times the beam radius away from the cavity centre with a larger gradient close to the cavity surface.

Studying hole features at various laser intensities, it is found that melting is always present for metal ablation as for copper at a pulse duration of 50 ns. Only a very narrow range of intensity ($1.0\text{--}1.8 \times 10^8 \text{ W cm}^{-2}$) was found to be dominated by vaporisation. Outside this range, molten metal motion develops gradually from being nearly stationary at low energy levels ($I < 3 \times 10^8 \text{ W cm}^{-2}$) to smooth flows at medium energy levels ($3 \times 10^8 \text{ W cm}^{-2} < I < 8 \times 10^8 \text{ W cm}^{-2}$) and to turbulent flows at high energy levels ($I > 8 \times 10^8 \text{ W cm}^{-2}$).

Figure 5 shows SEM micrographs of typical laser drilled holes. Figures 5(a) and 5(b) are holes drilled at $I = 6 \times 10^8 \text{ W cm}^{-2}$ using 10 pulses and 50 pulses, respectively. Figures 5(c) and 5(d) are holes drilled at $I = 2.5 \times 10^9 \text{ W cm}^{-2}$ using 10 pulses and 50 pulses, respectively. In both cases, samples were electropolished by about $0.15 \text{ }\mu\text{m}$ for Figs 5(a) and 5(b) and $0.4 \text{ }\mu\text{m}$ for Figs 5(c) and 5(d). Holes drilled at $2.5 \times 10^9 \text{ W cm}^{-2}$ show effects of stronger fluid motion than holes drilled at $6 \times 10^8 \text{ W cm}^{-2}$. The recast layers of the holes are clearly seen. At $6 \times 10^8 \text{ W cm}^{-2}$ the heat affected zones (HAZ) of the holes are around $1 \text{ }\mu\text{m}$, whereas at $2.5 \times 10^9 \text{ W cm}^{-2}$ the heat affected zones expand to more than $3 \text{ }\mu\text{m}$. The surface quality of the holes at $6 \times 10^8 \text{ W cm}^{-2}$ is slightly better than that at $2.5 \times 10^9 \text{ W cm}^{-2}$. The diameters of the holes changed from $3.3 \text{ }\mu\text{m}$ at $6 \times 10^8 \text{ W cm}^{-2}$ to $7.3 \text{ }\mu\text{m}$ at $2.5 \times 10^9 \text{ W cm}^{-2}$, whereas they remain almost the

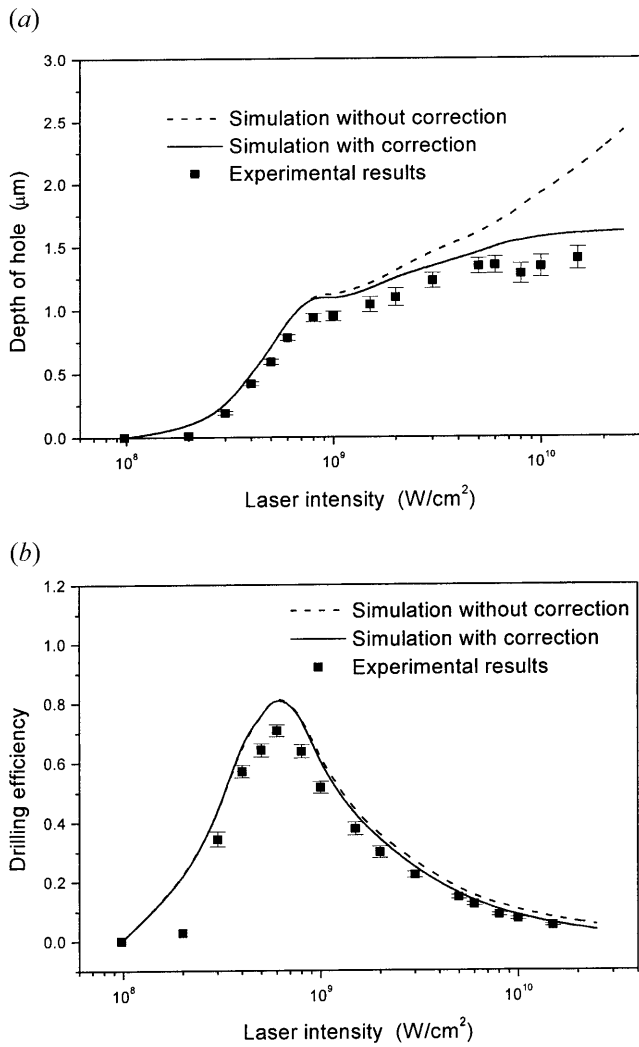


Fig. 6. (a) Drilling depth per pulse; (b) drilling efficiency. Wavelength $\lambda = 355 \text{ nm}$, Gaussian beam, beam radius $b = 2.25 \mu\text{m}$, pulse duration 50 ns , Cu.

same for 10 pulses and 50 pulses at the same energy level. Thus, choosing the suitable laser energy level is important for reducing drilling diameters and this diameter is relatively stable for more than 10 pulses.

Figure 6(a) shows the relationship between the depth of the hole and the laser intensity. Both simulation and experiments show that although vaporisation starts at $I > 0.98 \times 10^8 \text{ W cm}^{-2}$, obvious vaporisation starts at energy levels higher than $2 \times 10^8 \text{ W cm}^{-2}$. Ablation depth per pulse increases with intensity, but at higher intensities ($I > 2 \times 10^9 \text{ W cm}^{-2}$) the slope levels off. This is primarily due to plasma effects and part of the laser energy is absorbed and dissipated by the plasma. For laser intensity higher than $5 \times 10^8 \text{ W cm}^{-2}$, plasma effect correction is necessary for the simulation model (Eq. (3)). It is shown in Fig. 6(a) that simulation with correction agrees with the experimental data better than simulation without correction, especially when the laser intensity is higher than $1 \times 10^9 \text{ W cm}^{-2}$. Experimental drilling depth per pulse is lower than the simulation results. This is probably due to

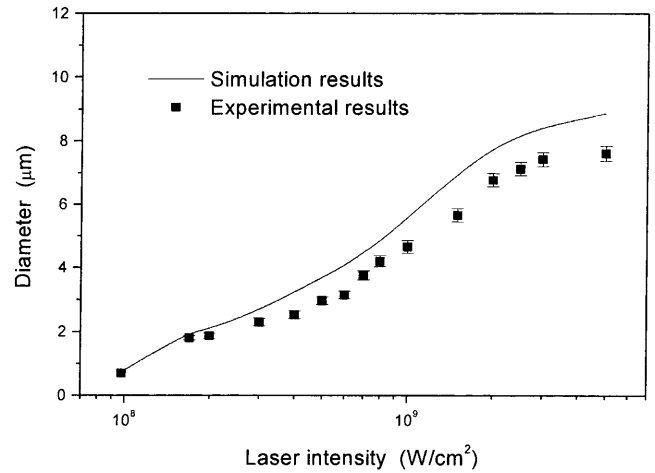


Fig. 7. Single pulse drilled hole diameters vs. laser intensity. Wavelength $\lambda = 355 \text{ nm}$, Gaussian beam, beam radius $b = 2.25 \mu\text{m}$, pulse duration 50 ns , Cu.

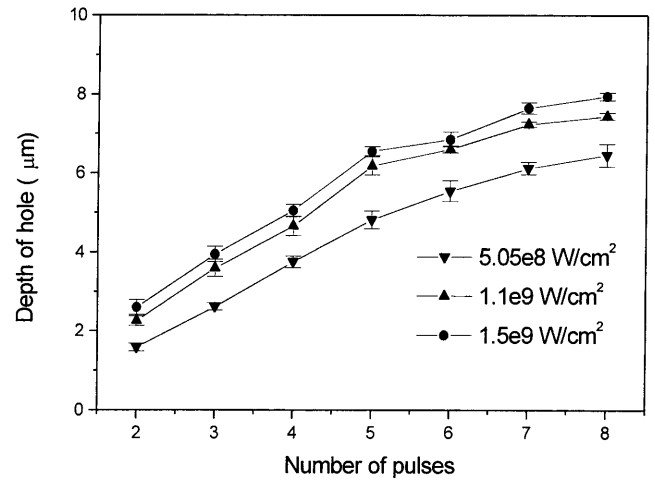


Fig. 8. Depth of holes at different energy levels vs. number of pulses. Beam radius $2.25 \mu\text{m}$, pulse duration 50 ns , repetition rate 2 kHz , Cu.

the neglect of radiation heat losses. Another reason is that the experimental data is the average of multi-pulse drilling depth. The saturation of drilling depth for multi-pulses is shown in Fig. 8.

Figure 6(b) shows how the drilling efficiency varies with laser intensity. Drilling efficiency is defined as [3]:

$$\eta = \frac{[L_m + L_v + c_p(T_v - T_0)]X}{(1 - RI)I}$$

where T_0 is the initial temperature, X is the ablation depth per pulse, $(1 - RI)I$ is the absorbed laser energy. Peak efficiency of 0.837 is reached at $6.0 \times 10^8 \text{ W cm}^{-2}$. Drilling efficiency is above 50% in the range of $3.35 \times 10^8 \text{ W cm}^{-2} \sim 1.95 \times 10^9 \text{ W cm}^{-2}$. Figure 6(b) also shows that drilling efficiency with plasma effects correction agrees with experimental data better than without correction. Figure 7 shows how the diameters of holes increase with laser intensities. Shrinkage in the cooling stage causes smaller holes than the estimated values, so

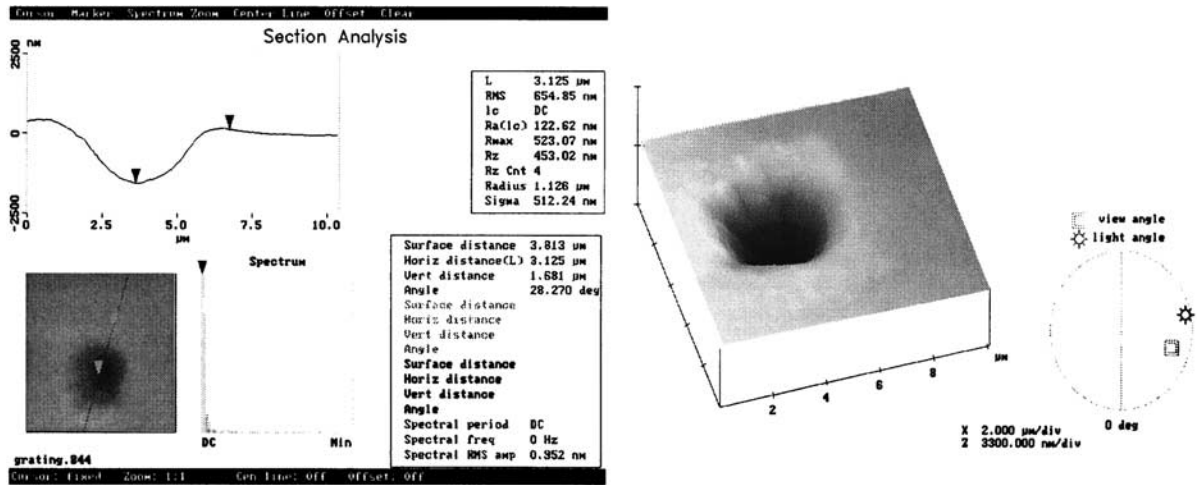


Fig. 9. AFM analysis of a hole drilled by 2 pulses at $6 \times 10^8 \text{ W cm}^{-2}$ Wavelength $\lambda = 355 \text{ nm}$, Gaussian beam, beam radius $b = 2.25 \text{ μm}$, Cu.

experimental diameters of holes are smaller than the simulation results. At intensities less than $1 \times 10^9 \text{ W cm}^{-2}$ this difference is small, at higher intensities the diameters level off. This figure shows that below $5 \times 10^9 \text{ W cm}^{-2}$ the fluid motion is relatively weak for the model to be effective. Beyond $5 \times 10^9 \text{ W cm}^{-2}$, recoil pressure and strong fluid motion effects must be considered to give satisfactory predictions of the diameters of holes. Simulations also show that hole diameters could be up to twice the focused beam size.

Figure 8 shows the relationship between the drilling depth and the number of pulses at three energy levels. The depth of hole increases with the number of pulses, but after 5 pulses this increase deviates from the linear relationship. The reason is that defocusing of laser beam and changes of cavity shape take effect. So real-time focus control is necessary for precision deep-hole drilling. Figure 9 shows the AFM analysis of a hole feature. The hole is drilled by two laser pulses at $6 \times 10^8 \text{ W cm}^{-2}$. The profile is smooth and shallow, the depth is 1.681 μm and the diameter is 4.4 μm .

Figure 10 shows the simulation results of the surface recess velocity distribution along the radial direction at $I = 6 \times 10^8 \text{ W cm}^{-2}$. The velocity distribution clearly reflects the effect of Gaussian beam intensity distribution. The central velocity increases with time but saturates after 30 ns. The distributions at 10 ns and 20 ns are relatively flat. The difference of the velocity distributions at different times is due to the change of cavity shape that alters the absorption of laser energy in the irradiated area. With time, the central area absorbs more energy than the surrounding areas, and the cavity becomes deeper and steeper. The recess velocities increase with time owing to continuous energy accumulation within the pulse duration period, but the profile does not expand proportionally. Since the increase in the central area is larger than that in the other areas, the central area deepens faster than the surrounding area. This explains the tapering phenomenon in laser drilling.

Figure 11 shows how the surface recess velocity at the centre of the hole changes with time at three energy levels. At $3 \times 10^8 \text{ W cm}^{-2}$, surface recess velocity is nearly zero before $t = 15 \text{ ns}$. It then starts increasing almost linearly with time. At $6 \times 10^8 \text{ W cm}^{-2}$, the dead zone is less than 5 ns,

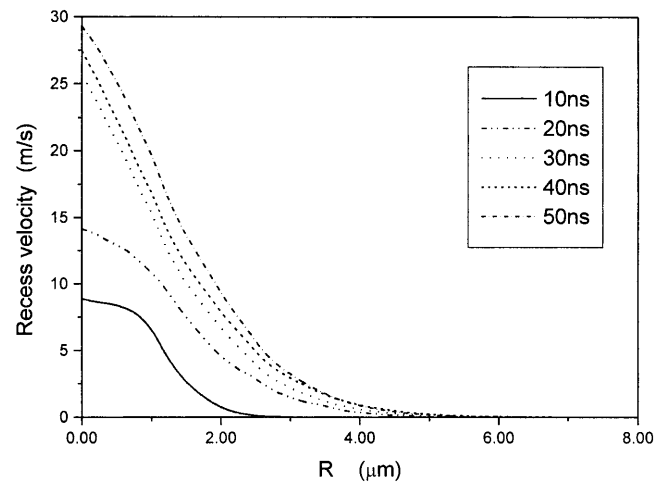


Fig. 10. Surface recess velocity at $6 \times 10^8 \text{ W cm}^{-2}$ Wavelength $\lambda = 355 \text{ nm}$, Gaussian beam, beam radius $b = 2.25 \text{ μm}$, pulse duration 50 ns, Cu.

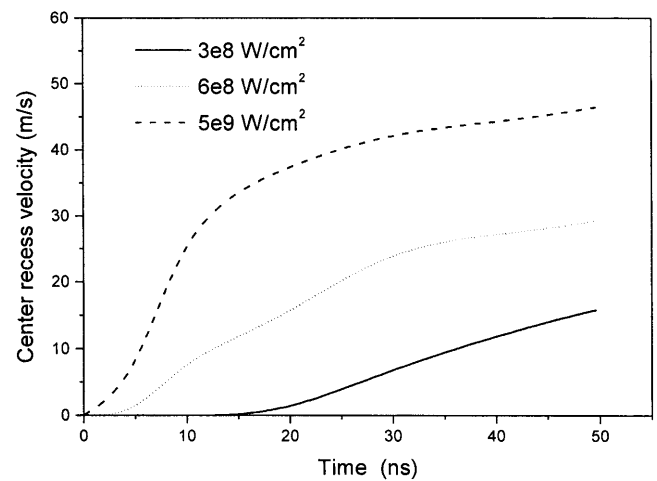


Fig. 11. Surface recess velocity at the center of the hole at three energy levels Wavelength $\lambda = 355 \text{ nm}$, Gaussian beam, beam radius $b = 2.25 \text{ μm}$, pulse duration 50 ns, Cu.

the velocity rises linearly up to about 30 ns, and then levels off. At $5 \times 10^9 \text{ W cm}^{-2}$ the velocity has a steeper rate of increase up to 10 ns and then levels off. The saturation at high intensities happens earlier than that at lower intensities.

The melt thickness at the cavity centre changes with laser intensity, as shown in Fig. 12. At low intensities fluid motion is weak, molten metal stays in the original locations, and the molten layer is thick. The melt thickness is about $0.5 \mu\text{m}$. The thickness decreases with the increase of laser intensity and reaches a minimum value of $0.28 \mu\text{m}$ at $4.7 \times 10^8 \text{ W cm}^{-2}$. After this value, the melt thickness increases again with laser intensity and saturates at a thickness of $0.42 \mu\text{m}$ after $2 \times 10^9 \text{ W cm}^{-2}$. The decrease at the middle range is due to a balance of vaporisation, external fluid motion and thermal conduction. At high intensities, the stronger heat flux causes an increase in the melting range. This range saturates when an energy balance with the outside is reached. The ratio of melt thickness at the centre to the diameter of the hole decreases constantly, and reaches a nearly steady value of 0.054 after $7 \times 10^8 \text{ W cm}^{-2}$. The ratio of melt thickness (in μm) to normalised laser intensity ($I/10^8$), Y , also decreases with laser intensity I (in W cm^{-2}), the relationship between Y and I can be expressed using the Lorentz function

$$Y - 0.02259 = \frac{7.3225 \times 10^7}{259267348 + 4(I - 1.451 \times 10^7)^2 + 259267348^2} \quad (10)$$

From Eq. (10) the melt depth at the centre can be predicted

$$\text{Depth} = 0.02259 \times \frac{I}{10^8} + \frac{0.73225 \times 259267348 \times I}{4(I - 1.451 \times 10^7)^2 + 259267348^2} \quad (11)$$

Equation (11) is valid when laser intensity is less than $1 \times 10^9 \text{ W cm}^{-2}$.

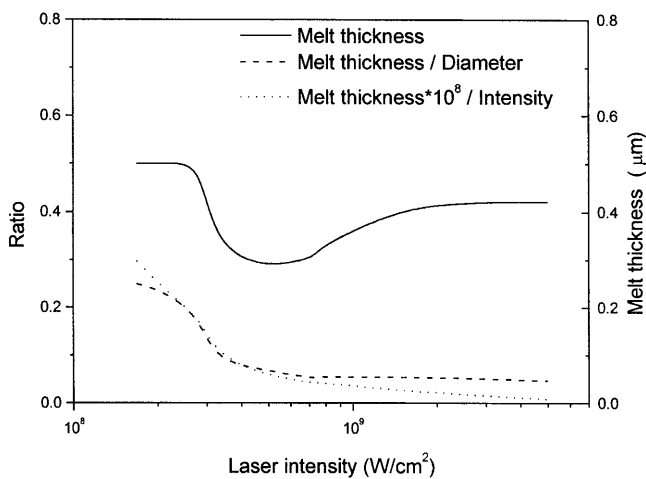


Fig. 12. Melt thickness at the center of holes (Righthand axis) and the two ratios (Lefthand axis) Wavelength $\lambda = 355 \text{ nm}$, Gaussian beam, beam radius $b = 2.25 \mu\text{m}$, pulse duration 50 ns, Cu.

6. Concluding Remarks

The physical aspects of UV laser micromachining of copper are discussed. A numerical model to simulate the microscale cavity formation under a high-intensity, pulsed laser irradiation is provided. The simulation results of UV laser machining of copper at nanosecond and micron scales are presented and compared with experimental results. Drilling depth and hole diameter for a wide range of laser intensities are predicted for $\lambda = 355 \text{ nm}$ and 50 ns pulse duration. Results show that melting of copper starts at around $6 \times 10^7 \text{ W cm}^{-2}$, vaporisation at around $1.06 \times 10^8 \text{ W cm}^{-2}$, and obvious vaporisation at $2 \times 10^8 \text{ W cm}^{-2}$. Fluid flow is relatively weak below $1 \times 10^9 \text{ W cm}^{-2}$ and plasma effects and gas dynamic effects should be considered at high intensities ($I > 5 \times 10^9 \text{ W cm}^{-2}$). Only a very narrow range (1.06×10^8 to $1.8 \times 10^8 \text{ W cm}^{-2}$) of vaporisation dominated ablation exists for such nanosecond lasers.

Acknowledgements

Financial support from NSF under grant DMI-9813453 and equipment support from ESI are gratefully acknowledged. Assistance by Professor Xuanhui Lu in setting up the experiments is also acknowledged. Assistance with AFM/SEM measurements and electropolishing rendered by Dr Adrian Campbell, Dr Alex Limanov and Dr Yang Cao is appreciated.

References

1. H. Hayashi and I. Miyamoto, "Process of thin Cu film removal by KrF excimer laser", ICALCO'95, pp. 391–400, 1995.
2. H. E. Hunger, H. Pietsch, S. Petzoldt and E. Matthias, "Thin film selective multishot ablation at 248 nm", SPIE Lasers in Microelectronic Manufacturing, 1598, pp. 19–26, 1991.
3. W. W. Duley, UV Lasers: Effects and Applications in Material Science, Cambridge University Press, 1996.
4. U. C. Paek and F. P. Gagliano, "Thermal analysis of laser drilling processes", IEEE Journal of Quantum Electronics, QE-8, pp. 112–119, 1972.
5. F. W. Dabby and U. C. Paek, "High-intensity laser-induced vaporization and explosion of solid material", IEEE Journal of Quantum Electronics, QE-8(2), pp. 106–111, 1972.
6. J. R. Ho, C. P. Grigoropoulos and J. A. C. Humphrey, "Computational model for the heat transfer and gas dynamics in the pulsed laser evaporation of metals", Journal of Applied Physics, 78(7), pp. 4696–4709, 1995.
7. A. Kar and M. Mazumder, "Mathematical model for laser ablation to generate nanoscale and submicrometer-size particles", Journal of Physical Review E, 49(1), pp. 410–419, 1994.
8. M. F. Modest, "Three-dimensional, transient model for laser machining of ablating decomposing materials", International Journal of Heat Mass Transfer, 39(2), pp. 221–234, 1996.
9. M. Aden, E. Beyer, G. Herziger and H. Hunze, "Laser-induced vaporization of a metal surface", Journal of Physics, D 25, pp. 57–65, 1992.
10. R. K. Singh and J. Narayan, "Pulsed-laser evaporation technique for deposition of thin films: physics and theoretical model", Physics Review B 41(3), pp. 8843–8859, 1990.
11. M. V. Sussman, Elementary General Thermodynamics, Addison-Wesley, New York, 1992.
12. C. J. Knight, "Theoretical modeling of rapid surface vaporization with back pressure", AIAA Journal, 17(5), pp. 519–523, 1979.

13. T. D. Bennett, D. J. Krajnovich, C. P. Grigoropoulos, P. Baumgart and A. C. Tam, "Marangoni mechanism in pulsed laser texturing of magnetic disk-substrates", *Journal of Heat Transfer*, 119, pp. 589–596, 1997.
14. V. R. Voller and C. Prakash, "A fixed grid numerical modeling methodology for convection–diffusion mushy region phase-change problems", *International Journal of Heat Mass Transfer*, 30(8), pp. 140–145, 1987.
15. Orazio Svelto, *Principles of Lasers*, 4th edn, New York, Plenum Press, pp. 148–158, 1998.
16. W. M. Steen, *Laser Material Processing*, pp. 80–89, Springer-Verlag, London, 1994.
17. I. Ursu, I. N. Mihilescu and Al. Popa et al. "Studies of the change of a metallic surface microrelief as a result of multiple-pulse action of powerful UV laser pulses", *Journal of Applied Physics*, 58(10), pp. 3909–3913, 1985.
18. I. S. Grivoriev and E. Z. Meilikhov. *Handbook of Physical Quantities*, New York, CRC Press, 1997.

Appendix

1. *Computation of penetration depth of copper.* The characteristic penetration depth of UV laser in metals is $\lambda/4\pi k$, where k is the distinction refractive index of target material, and λ is the laser wavelength. For copper, $k = 1.93$ if $\lambda = 355$ nm, and penetration depth is 14.6 nm.
2. *Computation of internal energy fluctuation.* If U is the internal energy, the internal energy fluctuation is $\Delta U/U$. From thermodynamics, $\Delta U/U \cong (3N)^{-1/2}$, where N is the number of atoms in the acting volume. For copper–laser interaction at 355 nm and 4.5 μm beam radius, penetration depth is 14.6 nm. Copper atom diameter is 3.54×10^{-10} m. Then, $\Delta U/U \cong 2.44 \times 10^{-9}$ [3].
3. *Some reference values for copper–laser interaction.* The melting threshold of copper at 308 nm and 40 ns is 5×10^7 W cm^{-2} [17]. The threshold for plasma formation can be calculated using $I_c = 1.1 \times 10^9 T_v/m\lambda^2$, where T_v is the vaporisation temperature in Kelvin, m is the average atomic mass, λ is the wavelength in μm . For copper at 355 nm, $I_c = 5 \times 10^8$ W cm^{-2} . Strong plasma formation for copper happens at $I_{strong} = 5 \times 10^9$ W cm^{-2} [3].
4. *Properties of copper used in this paper.* Density $\rho = 8960$ kg m^{-3} , melting temperature $T_m = 1083^\circ\text{C}$, latent heat of melting $L_m = 13.0$ kJ mol^{-1} at 1atm., vaporisation temperature $T_v = 2543^\circ\text{C}$, and latent heat of vaporisation $L_v = 302$ kJ mol^{-1} at 1atm. Other thermal properties of copper are treated as temperature sensitive and are interpolated from tabulated data in order to obtain reasonable calculation results [18]. The isotropic specific heat capacity is given by

$$c_p(T) = 116.0\ln(T) - 31.8.27 \quad (12)$$

The thermal conductivity for solid copper is

$$k(T) = 406.375 - 0.02241T - 3.13091 \times 10^{-5} T^2 + 4.521 \times 10^{-9} T^3 \quad (13)$$

and for liquid copper

$$k(T) = 27.892 + 0.17392T - 6.39142 \times 10^{-5} T^2 + 7.74766 \times 10^{-9} T^3 \quad (14)$$

Nomenclature

b	beam radius
C	plasma correction coefficient
c_p	heat capacity
D_0	beam waist
DOF	depth of focus
D_{min}	minimum focused spot size
E_v	gas energy
H	The enthalpy of the material
ΔH	latent heat
h	sensible heat
I	laser intensity
I_c	threshold laser intensity for plasma formation
I_{strong}	laser intensity for strong plasma formation
k	heat conductivity/extinction coefficient
L_m	latent heat of melting
L_v	latent heat of vaporisation
M^2	laser beam quality
Ma_v	vapour Mach number
M_v	molecular mass of vaporised particles
n	index of refraction
Q	laser heat flux
R	universal gas constant
Rl	reflectivity
r	distance along radial direction
T	temperature
T_0	initial temperature
t	time
U	internal energy
$\Delta U/U$	internal energy fluctuation
v	velocity
x	distances along axial direction
X	ablation depth per pulse
Y	ratio of melt thickness to normalised laser intensity
Z_0	beam waist location
α	heat diffusivity
β	laser absorptivity
γ	specific heat ratio
λ	wavelength
ρ	density
$\theta_{infinity}$	divergence at large distance
τ_e	electron relaxation time
$\tau_{lattice}$	time of energy transfer from electron to lattice
η	drilling efficiency

Subscripts

v	vapour phase
l	liquid phase
i	melt–vapour interface
vi	vapour adjacent to the Knudsen layer
li	liquid adjacent to the Knudsen layer